Misdetection Risk-aware Adaptive LiDAR Sensing for Automotive Driving

Chris Hogendoorn*, Ruben Wosten*, Marnix Zimmerman*, Nitin Jonathan Myers
*Equal contributors to the article
Delft Center for Systems and Control, Delft University of Technology, The Netherlands
Email: {c.a.g.hogendoorn, h.r.b.wosten, m.a.e.zimmerman, n.j.myers}@tudelft.nl

2025 IEEE 101st Vehicular Technology Conference (VTC2025-Spring) | 979-8-3315-3147-8/25/$31.00 ©2025 IEEE | DOI: 10.1109/VTC2025-SPRING65109.2025.11174409

***Abstract*—Automotive LiDARs typically have a uniform scanning range over their field of view (FoV). Such a range profile does not account for the varying risk of misdetecting targets in different regions. For instance, prioritizing crosswalks in a LiDAR scan is crucial, as the financial consequences of missing a pedestrian far exceed that of overlooking a distant vehicle. In this paper, we construct a spatial risk map that quantifies the risk of misdetecting targets across different regions around the vehicle. Our risk map incorporates lane semantics, knowledge about previously identified objects, and their potential trajectories. We use this risk map to adapt the LiDAR's scanning range over different sectors in its FoV. Simulations on nuScenes episodes demonstrate that our misdetection risk-aware design reduces the effective risk by about 40% compared to a standard LiDAR.**

***Index Terms*—Adaptive LiDAR, Semantics, Lane topology.**

I. Introduction

Light Detection and Ranging (LiDAR) is used in automotives to acquire a 360° perception of its surroundings [1]. To achieve this perception, a LiDAR emits laser pulses in different directions using a spinning platform [2] or with microelectromechanical mirrors [3]. The laser pulse reflections are used to determine the range of targets along different directions. The targets identified by a LiDAR are represented as a point in a point cloud representation of the environment.

Automotive LiDARs typically scan the environment homogeneously in their field of view (FoV). This results in a uniform range and resolution profile over the FoV, which may be suboptimal when side-information on the environment is available [4]–[6]. To address this issue, prior work has developed adaptive LiDARs that dynamically tailor their scanning profile to the context. The context was determined from a co-located camera in [4], past LiDAR scans in [5], and location-based street maps in [6]. For example, the system in [6] adapts the LiDAR's range and resolution across different sectors in the FoV. Existing adaptive LiDAR techniques, however, do not explicitly account for the risk due to failing to detect targets.

The risk associated with an automotive misdetecting a target depends on several factors including lane semantics [7], speed of the ego vehicle, type of targets, and their trajectories [8]. In this paper, we partition the space around an automotive into a rectangular grid of cells. Each cell is assigned a risk, which is a combination of a static risk and a real-time risk. The static risk depends solely on the lane semantics (e.g., cells on crosswalks have a higher risk than the others). The real-time risk depends on the objects detected in the most recent scan of the environment and their future trajectories. We propose a spatial risk map at an automotive based on the lane semantics as well as the dynamics of objects in the environment.

An automotive LiDAR can leverage our proposed spatial risk map at its location to emphasize scanning cells associated with a higher risk. This can be achieved by adapting the LiDAR's range and resolution to the risk map. In this paper, we focus only on range adaptation by optimizing the power transmitted by the LiDAR in different angular sectors within its FoV. By intelligently distributing the power in different sectors, the probability of scanning high risk cells is enhanced with our design. We evaluate our LiDAR power profile optimization technique on driving episodes from the nuScenes dataset [9]. A video showing the evolution of the risk map and the LiDAR point cloud using our method is available online[1].

II. Overview of the proposed system

The proposed system partitions the 360° FoV of the LiDAR into N distinct sectors of equal width. The sectors are illustrated in Fig. 1b for $N = 8$. We define P_i as the power emitted by the LiDAR's laser in the i^{th} sector and P_{avg} as the average power emitted over the 360° FoV, i.e.,

$$\frac{1}{N}\sum_{i=1}^{N} P_i = P_{\text{avg}}. \tag{1}$$

Here, P_i determines the probability of the LiDAR successfully detecting a target at a specified distance in the i^{th} sector. While a standard LiDAR typically employs $P_i = P_{\text{avg}}\,\forall i$, the proposed LiDAR uses a power profile that is tailored to the misdetection risk map at the ego vehicle's location. The misdetection risk at a cell in the environment is a measure of the collision risk due to failing to detect a target at that cell.

To construct the misdetection risk map, we discretize a rectangular region around the ego vehicle into an $N_{\text{x}} \times N_{\text{y}}$ cartesian grid with a resolution of δ along both dimensions. At the location (x, y) on this grid, we define $R_{\text{semantic}}(x, y)$ as the lane semantics-based risk, $R_{\text{timelapse}}(x, y)$ as the risk due to the time elapsed since the cell was last scanned, and $R_{\text{dynamics}}(x, y)$ as the risk associated with missing a previously identified object. These three risk maps vary spatially but they do not account for the ego vehicle's speed, denoted by v_{ego}. For example, $R_{\text{semantic}}(x, y)$ is the same for

[1]https://github.com/nitinjmyers/RiskAwareLiDAR

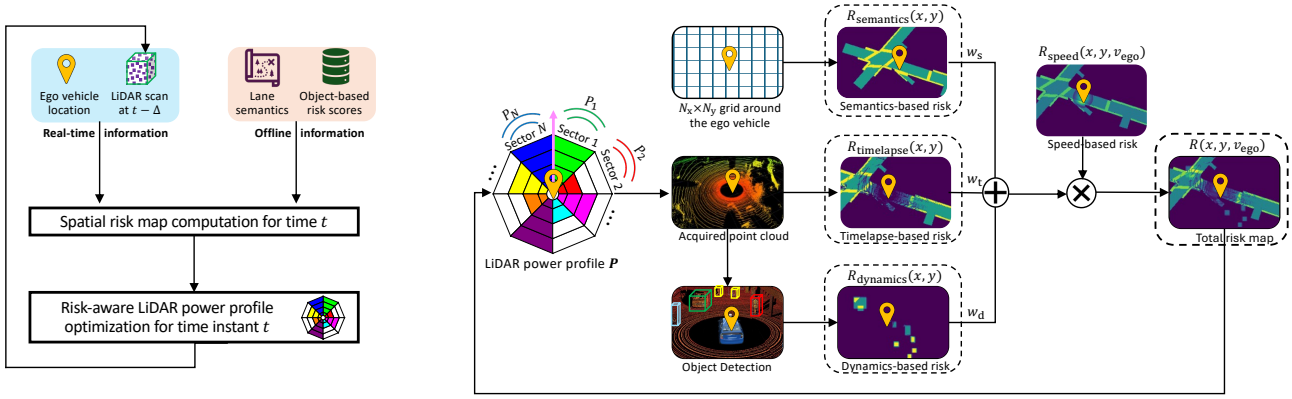

(a) Overview of our risk-aware adaptive LiDAR

(b) Schematic illustrating different blocks in our risk-aware adaptive LiDAR

Fig. 1: Our LiDAR optimizes the power profile $\mathbf{P}$ to minimize the total misdetection risk at the ego vehicle's location. The i^{th} entry of $\mathbf{P}$, i.e., P_i, is the power emitted in sector i. The point cloud obtained with $\mathbf{P}$ is used to update risk for the next scan.

all (x, y)s on a crosswalk, regardless of their distance from the ego vehicle. However, the risk associated with missing a pedestrian must be higher when the pedestrian is closer to the ego vehicle. To incorporate speed dependence, we include a correction factor $R_{\text{speed}}(x, y, v_{\text{ego}})$, which is the estimated time-of-arrival-based risk introduced in [10].

Our total misdetection risk at (x, y), denoted by $R(x, y, v_{\text{ego}})$, is based on a weighted combination of the risks $R_{\text{semantic}}(x, y)$, $R_{\text{dynamics}}(x, y)$, and $R_{\text{timelapse}}(x, y)$. We define the corresponding weights as w_{s}, w_{d}, and w_{t} to write

$$R(x, y, v_{\text{ego}}) = R_{\text{speed}}(x, y, v_{\text{ego}}) \times \Big[w_{\text{s}} R_{\text{semantic}}(x, y) + w_{\text{d}} R_{\text{dynamics}}(x, y) + w_{\text{t}} R_{\text{timelapse}}(x, y) \Big]. \quad (2)$$

The risk factors in (2) are time-dependent; for notational simplicity, we omit the explicit time variable, though its dependence is implicitly understood. Here, $R_{\text{timelapse}}(x, y)$ and $R_{\text{dynamics}}(x, y)$ depend on the past LiDAR scans, while $R_{\text{semantic}}(x, y)$ depends solely on the static lane topology. These risk components and the total risk are shown in Fig. 1b for a particular snapshot in a driving scenario.

Our proposed approach, illustrated in Fig. 1a, integrates risk map construction, adaptive LiDAR sensing, and object tracking in a closed-loop. We now describe how this loop operates and discuss the risk factors in the following sections. At the start, since no real-time point cloud data is available, our system relies solely on lane semantics-based risk $R_{\text{semantic}}(x, y)$ and ego vehicle speed-based risk $R_{\text{speed}}(x, y, v_{\text{ego}})$ to adapt LiDAR sensing. Thus, for the first scan, we set $w_{\text{t}} = 0$ and $w_{\text{d}} = 0$ in (2). The resulting total risk map $R(x, y, v_{\text{ego}})$ is then used to optimize the LiDAR's power profile via our algorithm in Sec. IV. Then, an initial point cloud of the environment is acquired using the optimized LiDAR profile, completing the first iteration. This acquired point cloud enables the construction of real-time risk maps $R_{\text{timelapse}}(x, y)$ and $R_{\text{dynamics}}(x, y)$ for the next iteration. At this stage, w_{t} and w_{d} are assigned non-zero values, as defined by the user. The updated total risk map is then used to optimize the LiDAR's power profile to sense the next scene, and this process continues as shown in Fig. 1b.

III. Proposed Procedure to Construct Risk Map

In this section, we explain how we construct the risk factors within our total risk map $R(x, y, v_{\text{ego}})$ in (2).

Lane semantics-based risk: The cells around an ego vehicle can be categorized into different types, such as lanes, sidewalks, crosswalks, or areas occupied by static obstacles. This classification is feasible today using street maps that provide information on lane semantics. In this paper, we consider only two classes within the drivable space for simplicity: (i) the *Pedestrian-Accessible Zone (PAZ)*, where pedestrians may be present and (ii) the *Vehicle-Only Zone (VOZ)*, where only other vehicles may be present and pedestrians are forbidden. We set $R_{\text{semantic}}(x, y)$ to the collision costs with the most vulnerable object that can occur at (x, y). As the impact is typically higher for collisions with pedestrians, we write

$$R_{\text{semantic}}(x, y) = \begin{cases} R_{\text{ped}}, & (x, y) \in \text{PAZ} \\ R_{\text{veh}}, & (x, y) \in \text{VOZ} \end{cases}, \quad (3)$$

where R_{ped} and R_{veh} represent the expected costs of collisions with pedestrians and vehicles. A sketch of $R_{\text{semantic}}(x, y)$ for one driving snapshot in nuScenes is shown in Fig. 1b.

Target dynamics-based risk: We compute $R_{\text{dynamics}}(x, y)$ at time instant t using point cloud data from the most recent LiDAR scan, taken at $t - \Delta$. An object detected in the scan at $t - \Delta$, represented by a bounding box in Fig. 2a, may follow multiple possible trajectories in a Δ interval. Prior work [11], [12] predicts these trajectories based on object dynamics and road topology, assigning probabilities to each possible path. An example showing such paths is illustrated in Fig. 2a. Using the predicted trajectories, the cells where the object can possibly appear at time t can be determined. A risk-aware LiDAR should emphasize scanning those cells where the object, initially detected at $t-\Delta$, is likely to appear.

We describe how to compute the risk of misdetecting an object that was already identified in a previous LiDAR scan. The probable coordinates of a previously identified object at the current time instant t, along with their associated probabilities, is obtained using a trajectory prediction algorithm. For an object indexed n, we construct an occupancy probability map $\mathbb{P}(x, y, n)$ at time t. This map represents the chance that the n^{th} identified object occupies the $(x, y)^{\text{th}}$ cell at time t. For the example in Fig. 2a, $\mathbb{P}(x, y, n)$ is set to 0.2 for all cells in the green bounding box and 0 otherwise. When there are areas of overlap between the predictions, the occupancy probabilities are summed up as shown in Fig. 2b.

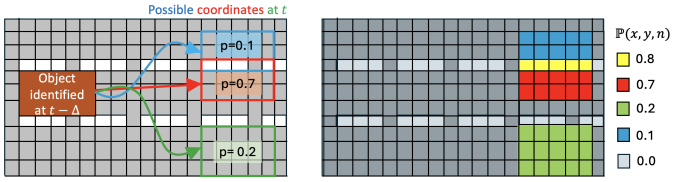

(a) Object trajectory prediction (b) Occupancy probability map at time t

Fig. 2: A trajectory prediction algorithm estimates the possible coordinates of an object at time t, based on its detected position at $t-\Delta$. These coordinates and the trajectory probabilities are used to construct the occupancy probability map.

The target dynamics-based risk map associated with the n^{th} object identified at $t - \Delta$ is defined as

$$R_{\text{dynamics}}(x, y, n) = \mathbb{P}(x, y, n) \times \text{Cost}(\text{ObjectClass}_n) \times \text{Cost}(\text{Orientation}_n|\text{ObjectClass}_n), \quad (4)$$

where $\text{Cost}(\text{ObjectClass}_n)$ quantifies the collision risk associated with an object type. The factor $\text{Cost}(\text{Orientation}_n|\text{ObjectClass}_n)$ depends on the object's orientation. While this factor is 1 for any orientation of a pedestrian, it varies when the tracked object is a vehicle. Studies in [13] indicate that collisions with vehicles moving perpendicular to the ego vehicle tend to be more severe than those involving other orientations. Therefore, the factor for such vehicle orientations is usually higher.

We explain how target dynamics-based risk is determined from trajectory predictions for multiple objects. Let $N_{\text{obj},t-\Delta}$ denote the number of objects detected in the LiDAR scan at time $t - \Delta$. For every object $n \in \{1, 2, 3, \cdots N_{\text{obj},t-\Delta}\}$, its dynamics-based risk map can be calculated according to (4). The dynamics-based risk map for the scene is defined as

$$R_{\text{dynamics}}(x, y) = \sum_{n=1}^{N_{\text{obj},t-\Delta}} R_{\text{dynamics}}(x, y, n), \quad (5)$$

which is just the sum of the dynamics-based risk maps associated with each identified object.

Risk due to timelapse: A LiDAR may not scan a certain cell in the environment due to its range or resolution limitation, or occlusion by targets in other cells. A cell unscanned in a previous LiDAR scan is a blind spot. Our timelapse-based risk map assigns low risk values at cells that were frequently scanned by a LiDAR, while unscanned areas, such as a new road after a turn, are assigned a higher risk.

Our timelapse-based risk at time t is defined as the product of a cell's lane semantic-based risk and its occupancy uncertainty (denoted by OCU), i.e.,

$$R_{\text{timelapse}}(x, y) = R_{\text{semantic}}(x, y) \times \text{OCU}(x, y, t). \quad (6)$$

Here, the OCU, which ranges between 0 and 1, increases when there is a significant time lapse since the cell was last scanned. Our method updates the OCU based on the timelapse as

$$\text{OCU}(x, y, t) = \begin{cases} [\text{OCU}(x, y, t-\Delta) - \beta]^+, \sum_z N_{\text{lidar}}(x, y, z; t-\Delta) > 0, \\ [\text{OCU}(x, y, t-\Delta) + \gamma]_1, \sum_z N_{\text{lidar}}(x, y, z; t-\Delta) = 0, \end{cases} \quad (7)$$

where β and γ are non-negative parameters controlling the OCU decrease and increase, and $N_{\text{lidar}}(x, y, z; t-\Delta)$ is the number of LiDAR points in (x, y, z) at $t - \Delta$. Since targets may not always be present in scanned cells, we make use of ground reflections in $\sum_z N_{\text{lidar}}(x, y, z; t-\Delta)$ to determine if the LiDAR scanned the cell (x, y). Finally, the operations $[q]^+ = \max(q, 0)$ and $[q]_1 = \min(q, 1)$ ensure that $\text{OCU}(x, y, t)$ always lies between 0 and 1.

Ego vehicle speed-based risk: The risks $R_{\text{timelapse}}(x, y)$, $R_{\text{dynamics}}(x, y)$, and $R_{\text{semantic}}(x, y)$ are all independent of the ego vehicle's speed. In practice, a high-speed ego vehicle has a shorter estimated time of arrival (ETA) to a given cell, which increases the risk in cases of misdetection. For simplicity, we disregard the direction of the ego vehicle's motion to write

$$\text{ETA}(x, y, v_{\text{ego}}) = \left(\sqrt{(x - x_{\text{ego}})^2 + (y - y_{\text{ego}})^2}\right) / v_{\text{ego}}, \quad (8)$$

where $(x_{\text{ego}}, y_{\text{ego}})$ is the ego vehicle coordinate and v_{ego} is its speed. This ETA is incorporated into the distance dependent risk expression proposed in [10], i.e., $R_{\text{speed}}(x, y, v_{\text{ego}}) = 0.0667\text{ETA}^3_{(x,y,v_{\text{ego}})} - 0.3\text{ETA}^2_{(x,y,v_{\text{ego}})} + 0.0333\text{ETA}_{(x,y,v_{\text{ego}})} + 1$ when $\text{ETA}_{(x,y,v_{\text{ego}})} \leq 3$ seconds and is 0.5 otherwise. An example of $R_{\text{speed}}(x, y, v_{\text{ego}})$ is illustrated in Fig. 1b.

Choice of risk weights: Our total risk in (2) scales the semantics-based, dynamics-based, and time lapse-based components differently. These weights can be dynamically adapted based on context. For instance, in high-traffic urban areas, increasing the dynamics-based risk weight would ensure that LiDAR scans emphasize traffic participants. Although we use fixed weights, adapting the weights to the environment is an interesting research direction that is beyond this paper's scope.

IV. Scanning with our Risk-Aware Adaptive LiDAR

We now discuss our method to optimize the power emitted by the LiDAR, i.e., $\mathbf{P} = \{P_i\}_{i=1}^N$, over the N sectors in its field of view. The emitted power influences the probability of successfully detecting a target at a cell in the environment. We denote this probability at a cell (x, y) as $P_{\text{d}}(x, y, \mathbf{P})$. The angle made by the position vector to $(x - x_{\text{ego}}, y_{\text{ego}})$ with the ego vehicle's heading direction determines the sector in which

(x, y) lies. We use $n_{(x,y)} \in [N] \triangleq \{1, 2, \cdots, N\}$ to denote its sector. For a Neyman-Pearson detector [14]

$$P_{\mathrm{d}}(x, y, \mathbf{P}) = 0.5\mathrm{erfc}\left(\sqrt{\ln P_{\mathrm{fa}}^{-1}} - \sqrt{\mathrm{SNR}(d_{x,y}, P_{n_{(x,y)}}) + 0.5}\right), \quad (9)$$

where P_{fa} is the false alarm rate and $d_{x,y}$ is the distance between the (x, y) cell and the ego vehicle at $(x_{\mathrm{ego}}, y_{\mathrm{ego}})$. The signal-to-noise ratio (SNR) depends on the power emitted by the LiDAR in sector $n_{(x,y)}$ and the target reflectivity, and its expression for an avalanche photodiode (APD)-based LiDAR detector is provided in [14]. In this paper, we use the APD parameters from [14] in the SNR expression.

The effective risk associated with the (x, y) cell is the product of the probability of failing to scan the cell and its total risk score, i.e.,

$$R_{\mathrm{effective}}(x, y, \mathbf{P}) = (1 - P_{\mathrm{d}}(x, y, \mathbf{P}))R(x, y, v_{\mathrm{ego}}). \quad (10)$$

This product is summed over all cells in the $N_{\mathrm{x}} \times N_{\mathrm{y}}$ grid to compute the total effective risk associated with the power profile $\mathbf{P}$. Emitting a high power in all directions results in a high received SNR, which increases $P_{\mathrm{d}}(x, y, \mathbf{P})$ and consequently reduces the effective risk in (10). In practice, however, the emitted power is limited due to the average power constraint in (1) and the admissible exposure limit (AEL). The admissible exposure limit (AEL) establishes the threshold at which laser emissions remain safe, preventing ocular damage to pedestrians near the ego vehicle.

We minimize the total effective risk at the ego vehicle, i.e., $\Sigma_x \Sigma_y R_{\mathrm{effective}}(x, y, \mathbf{P})$, by optimizing the LiDAR's power profile. The minimization is performed under the average power and the AEL constraints, and is formulated as

$$\begin{aligned} \min_{\mathbf{P}=\{P_i\}_{i=1}^{N}} \quad & \sum_{x=1}^{N_{\mathrm{x}}} \sum_{y=1}^{N_{\mathrm{y}}} R_{\mathrm{effective}}(x, y, \mathbf{P}) \\ \text{s.t.} \quad & \frac{1}{N} \sum_{i=1}^{N} P_i = P_{\mathrm{avg}}, \\ & P_i \leq P_{\mathrm{max}} \quad \forall i \in [N]. \end{aligned} \quad (11)$$

Here, P_{max} is the maximum power that the LiDAR can emit in any sector due to the AEL. We use the projected gradient descent algorithm to solve (11).

V. Simulation Results

To validate our method, we choose 7 distinct driving scenarios at random from the nuScenes dataset. Each scene lasts 20 seconds and comprises 40 samples of the driving simulation. Each sample corresponds to a snapshot of the environment, which is perceived using a LiDAR scan. As the samples are $20\mathrm{s}/40 = 0.5$ seconds apart, the time step $\Delta = 0.5\,\mathrm{s}$ in our simulations. The LiDAR's FoV is partitioned into $N = 8$ sectors. The region around the ego vehicle is discretized into a rectangular grid with $N_{\mathrm{x}} = 600$, $N_{\mathrm{y}} = 600$, and a spatial resolution of $\delta = 0.5\,\mathrm{m}$. We set $R_{\mathrm{ped}} = 1$ and $R_{\mathrm{veh}} = 0.552$ as per the studies in [15]- [16]. Furthermore, the risk factor weights are set to $w_{\mathrm{s}} = 1$, $w_{\mathrm{d}} = 2/\max\{R_{\mathrm{dynamics}}\}$ and $w_{\mathrm{t}} = 4/\max\{R_{\mathrm{timelapse}}\}$, prioritizing timelapse-based risk. The normalization by the maximum values ensure that the risks are comparable. The cost values we use in (4) are taken from [17] and [13], and are summarized in Tables I and II. The OCU parameters in (7) are set to $\beta = 1$ and $\gamma = 0.125$. Finally, we use $P_{\mathrm{max}} = 12\,\mathrm{W}$ [18] and $P_{\mathrm{fa}} = 10^{-4}$.

ObjectClass	Cost(ObjectClass)
Pedestrian	1.0
Barrier	0.567
Debris/ Traffic cone	0.556
Bicycle rack	0.718
Emergency vehicle/ Bicycle	1.0
Motor cycle/ Truck/ Bus	1.0
Trailer/ Car	0.90892

TABLE I: Collision cost factors from [17] are used in (4).

Orientation	Cost(Orientation|Vehicle)
front	0.8
side	1.0
rear	0.4

TABLE II: Orientation-based collision factors from [13].

In our simulations, we use the object trajectory prediction algorithm from [19] to update the dynamics-based risk in $R(x, y, v_{\mathrm{ego}})$. The map $R(x, y, v_{\mathrm{ego}})$ is used to minimize the total effective risk using (11) by optimizing the LiDAR's power profile. The optimized profile, defined as $\mathbf{P}_{\mathrm{opt}}$, is applied at the LiDAR to acquire a point cloud representation of the environment. In our simulations, we emulate the point cloud acquired with the optimized profile. To this end, we first generate a point cloud representation of the environment when the LiDAR operates at a high power (ignoring AEL) in all directions. The actual point cloud is then obtained by subsampling the high-power point cloud based on the optimized power profile. Specifically, only those LiDAR points at cells with $P_{\mathrm{d}}(x, y, \mathbf{P}_{\mathrm{opt}})) > 0.975$ are retained and the points at the remaining cells are discarded. This point cloud is then used to update the effective total risk for the next sample. This process repeats iteratively for the driving scene.

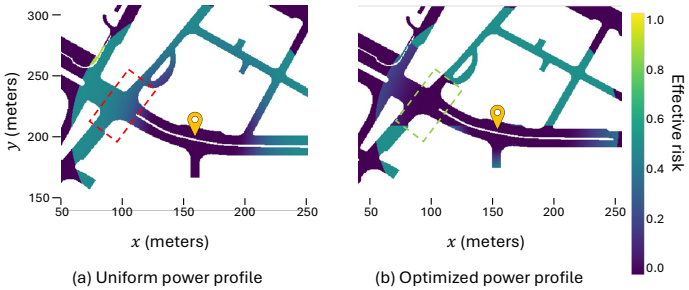

Fig. 3: The effective risk map in (10) with uniform and optimized power profiles, for sample 7 of scene 4 (nuScenes), when $P_{\mathrm{avg}} = 3\,\mathrm{W}$. The optimized profile reduces the effective risk in critical zones like the driving lane and intersections.

We discuss our results when the average power P_{avg} is increased from 3 W to 12 W in steps of 3 W. For a specific P_{avg} in this range, our optimization problem in (11) is solved

for each sample, i.e., 40 times in each of the 7 driving scenarios. The optimum power profile at the LiDAR changes as the total risk map evolves with time due to ego vehicle's motion. For a randomly chosen sample, Fig. 3 shows the spatial map of the effective risk $(1-P_{\mathrm{d}}(x,y,\mathbf{P}))R(x,y,v_{\mathrm{ego}})$ around the ego vehicle for our optimized profile $\mathbf{P}_{\mathrm{opt}}$ and the uniform profile $P_{\mathrm{avg}} \times \mathbf{1}$. Here, $\mathbf{1}$ is an $N \times 1$ vector of ones. Our optimized profile demonstrates a reduced effective risk along the driving lane compared to a uniform power profile. Additionally, it lowers the effective risk at intersections. These aspects are crucial in automotive driving, as targets in the driving lane and near intersections present a higher risk than those in distant lanes.

We now discuss the effective risk reduction achieved with our optimized power profile $\mathbf{P}_{\mathrm{opt}}$ over the uniform power profile $P_{\mathrm{avg}} \times \mathbf{1}$. The risk reduction percentage η is defined as

$$\eta = \frac{R_{\mathrm{effective}}(P_{\mathrm{avg}} \times \mathbf{1}) - R_{\mathrm{effective}}(\mathbf{P}_{\mathrm{opt}})}{R_{\mathrm{effective}}(P_{\mathrm{avg}} \times \mathbf{1})} \times 100. \quad (12)$$

Fig. 4 shows a box plot of the risk reduction factor η with our method at different average power levels. The box plots are obtained for 280 samples taken across the 7 scenes from the nuScenes dataset. When the average power $P_{\mathrm{avg}} = P_{\max}$, there is only one feasible power profile in the constraint set, i.e., the uniform power profile $\mathbf{P} = P_{\max} \times \mathbf{1}$. At such a high power, the optimized profile is same as a uniform profile and $\eta = 0$ as seen in Fig. 4. At low total transmit powers, our optimized profile emphasizes scanning high risk areas and achieves a lower effective risk than a uniform profile. From Fig. 4, we observe that our approach achieves a median risk reduction of approximately 42% at a average power of 6 W and around 50% at 9 W.

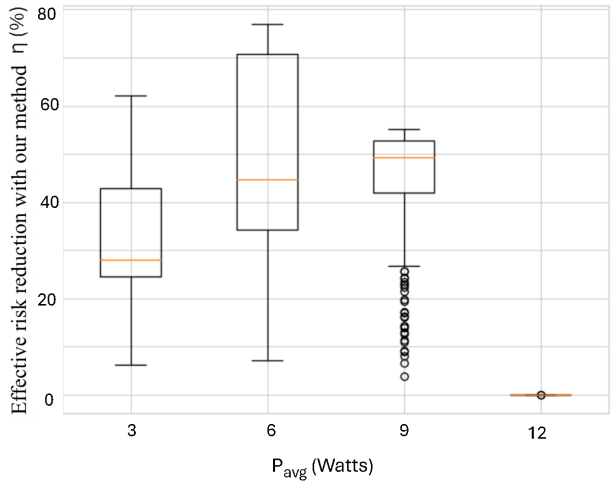

Fig. 4: Box plot based on 280 nuScenes samples shows that optimizing the LiDAR power profile using (11) results in a lower effective risk than a standard uniform power profile.

VI. Conclusions

This paper introduced the concept of a misdetection risk-aware adaptive LiDAR. Our approach prioritizes LiDAR scans in regions associated with higher risk around the ego vehicle. To this end, we propose a method for constructing a spatial risk map and an algorithm that adapts the LiDAR's scanning profile accordingly. The risk map is generated by incorporating scene semantics, past LiDAR scans, and the ego vehicle's speed. Through closed-loop simulations on the nuScenes dataset, we demonstrate that our risk-aware adaptive LiDAR improves detection along the driving lane and at intersections than a comparable standard LiDAR.

References

[1] R. Roriz, J. Cabral, and T. Gomes, "Automotive LiDAR technology: A survey," *IEEE Transactions on Intelligent Transportation Systems*, vol. 23, no. 7, pp. 6282–6297, 2021.

[2] Y. Li and J. Ibanez-Guzman, "Lidar for autonomous driving: The principles, challenges, and trends for automotive lidar and perception systems," *IEEE Signal Process. Mag.*, vol. 37, no. 4, pp. 50–61, 2020.

[3] H. W. Yoo, N. Druml, D. Brunner, C. Schwarzl, T. Thurner, M. Hennecke, and G. Schitter, "MEMS-based lidar for autonomous driving," *Elektrotechnik und Informationstechnik: e & i*, 2018.

[4] F. Pittaluga, Z. Tasneem, J. Folden, B. Tilmon, A. Chakrabarti, and S. J. Koppal, "Towards a MEMS-based adaptive lidar," in *IEEE Intl. Conf. on 3D Vision (3DV)*, pp. 1216–1226, 2020.

[5] T. Yamamoto, Y. Kawanishi, I. Ide, H. Murase, F. Shinmura, and D. Deguchi, "Efficient pedestrian scanning by active scan LIDAR," in *Intl. Workshop on Adv. Image Tech. (IWAIT)*, pp. 1–4, IEEE, 2018.

[6] T. Rhemrev, E. de Jong, G. van Triest, R. Kalkman, J. Pronk, A. Pandharipande, and N. J. Myers, "ELLAS: Enhancing LiDAR perception with location aware scanning profile adaptation," *IEEE Sensors Journal*, 2025.

[7] Y. Tan, N. Virani, B. Good, S. Gray, M. Yousefhussien, Z. Yang, K. Angeliu, N. Abate, and S. Sen, "Risk-aware autonomous navigation," in *Artificial Intelligence and Machine Learning for Multi-Domain Operations Applications III*, vol. 11746, pp. 335–348, SPIE, 2021.

[8] D. LaChapelle, T. Humphreys, L. Narula, P. Iannucci, and E. Moradi-Pari, "Automotive collision risk estimation under cooperative sensing," in *IEEE Intl. Conf. on Acoustics, Speech and Signal Process. (ICASSP)*, pp. 9200–9204, 2020.

[9] H. Caesar, V. Bankiti, A. H. Lang, S. Vora, V. E. Liong, Q. Xu, A. Krishnan, Y. Pan, G. Baldan, and O. Beijbom, "nuscenes: A multimodal dataset for autonomous driving," in *Proc. of the IEEE/CVF Conf. on Comput. Vision and Pattern Recog.*, pp. 11621–11631, 2020.

[10] J. Chen, W. Zhong, B. Gao, Y. Liu, H. Zou, J. Liu, Y. Lu, J. Huang, and Z. Zhong, "Risk occupancy: A new and efficient paradigm through vehicle-road-cloud collaboration," *arXiv preprint arXiv:2408.07367v2*, 2024.

[11] J. Wang, C. Guo, M. Guo, and J. Chen, "Jointly learning agent and lane information for multimodal trajectory prediction," in *26th IEEE International Conference on Pattern Recognition (ICPR)*, pp. 2921–2927, 2022.

[12] B. Kim, S. H. Park, S. Lee, E. Khoshimjonov, D. Kum, J. Kim, J. S. Kim, and J. W. Choi, "Lapred: Lane-aware prediction of multi-modal future trajectories of dynamic agents," in *Proc. of the IEEE/CVF Conf. on Comput. Vision and Pattern Recog.*, pp. 14636–14645, 2021.

[13] F. M. Abu-Zidan and H. O. Eid, "Factors affecting injury severity of vehicle occupants following road traffic collisions," *Injury*, vol. 46, no. 1, pp. 136–141, 2015.

[14] A. Nagai, C. Barry, S. Bellis, A. Browne, S. Buckley, E. Cashman, B. Couglan, S. Foley, and M. Perry, "Comparison of SPAD, SiPM and APD performance for ToF LiDAR application," in *Intl. SPAD Sensor Workshop (ISSW)*, 2024.

[15] K. Foppe, "What is the average car accident settlement amount?," January 2025. Brown & Crouppen Law Firm.

[16] R. Weinhaus, "What is the average payout for pedestrian hit by car?," February 2025. Brown & Crouppen Law Firm.

[17] A. Y. H. Stigson and A. Kullgren, "Variation in crash severity depending on different vehicle types and objects as collision partner," *International Journal of Crashworthiness*, vol. 14, no. 6, pp. 613–622, 2009.

[18] V. L. inc, "Hdl-32e datasheet," tech. rep., Velodyne Lidar, inc., 2018.

[19] J. Wang, C. Guo, M. Guo, and J. Chen, "Jointly learning agent and lane information for multimodal trajectory prediction," in *26th Intl. Conf. on Pattern Recog. (ICPR)*, pp. 2921–2927, 2022.